1   Continuous, Topologically Guided Protein Crystallization Controls Bacterial Surface Layer Self-

2   Assembly

3

4   Colin J. Comerci*[1,2], Jonathan Herrmann*[3,4], Joshua Yoon[5,2], Fatemeh Jabbarpour[3,4], Xiaofeng

5   Zhou[6], John F. Nomellini[7], John Smit[7], Lucy Shapiro[6], Soichi Wakatsuki[3,4], and W.E.

6   Moerner[1,2,5]

7

8   [1]Biophysics Program, Stanford University, Stanford, CA, USA

9   [2]Department of Chemistry, Stanford University, Stanford, CA, USA

10   [3]Department of Structural Biology, Stanford University, Stanford, CA, USA

11   [4]Bioscience Division, SLAC National Accelerator Laboratory, Menlo Park, CA, USA

12   [5]Department of Applied Physics, Stanford University, Stanford, CA, USA

13   [6]Department of Developmental Biology, Stanford University, Stanford, CA, USA

14   [7]Department of Microbiology and Immunology, University of British Columbia, Vancouver, BC,

15   CA

16

17   *These authors contributed equally to this work.

18

19   Abstract

20   Bacteria assemble the cell envelope using localized enzymes to account for growth and

21   division of a topologically complicated surface[1–3]. However, a regulatory pathway has not been

22   identified for assembly and maintenance of the surface layer (S-layer), a 2D crystalline protein

23   coat surrounding the curved 3D surface of a variety of bacteria[4,5]. By specifically labeling,

24   imaging, and tracking native and purified RsaA, the S-layer protein (SLP) from *C. crescentus*,

25   we show that protein self-assembly alone is sufficient to assemble and maintain the S-layer *in*

26   *vivo*. By monitoring the location of newly produced S-layer on the surface of living bacteria, we

27   find that S-layer assembly occurs independently of the site of RsaA secretion and that localized

28   production of new cell wall surface area alone is insufficient to explain S-layer assembly

29   patterns. When the cell surface is devoid of a pre-existing S-layer, the location of S-layer

30   assembly depends on the nucleation characteristics of SLP crystals, which grow by capturing

31   RsaA molecules freely diffusing on the outer bacterial surface. Based on these observations, we

32   propose a model of S-layer assembly whereby RsaA monomers are secreted randomly and

33   diffuse on the lipopolysaccharide (LPS) outer membrane until incorporated into growing 2D S-

34   layer crystals. The complicated topology of the cell surface enables formation of defects, gaps,

35   and grain boundaries within the S-layer lattice, thereby guiding the location of S-layer assembly

36   without enzymatic assistance. This unsupervised mechanism poses unique challenges and

37   advantages for designing treatments targeting cell surface structures or utilizing S-layers as self-

38   assembling macromolecular nanomaterials. As an evolutionary driver, 2D protein self-assembly

39   rationalizes the exceptional S-layer subunit sequence and species diversity[6].

40

41   Main Text

42   Assembling a macromolecular structure on the micron scale often requires input energy

43   and spatial coordination by enzymes and other cellular processes[1–3]. S-layers, however, exist

44   outside the cell envelope and lack access to many cytosolic components, including ATP[4–6]. How

45   do microbes continuously assemble a crystalline macromolecular structure on a highly curved

46   cell surface undergoing drastic changes during normal cell growth? To answer this question, we

47 performed time-resolved, super-resolution fluorescence imaging and single-molecule tracking

48 (SMT) of S-layer assembly on living *C. crescentus* cells. In *C. crescentus*, the S-layer is made of

49 a single 98 kDa SLP, RsaA, which accounts for around 30% of the cell's total protein synthesis[7].

50 RsaA, like other SLPs, self-assembles into crystalline sheets upon the addition of divalent

51 calcium (Ca^{2+}) *in vitro*[8–12]. Given the many fitness-related functions ascribed to crystalline

52 bacterial S-layers, we hypothesized that SLP self-assembly may play a role in generating the S-

53 layer coat *in vivo*[4,6].

54   RsaA covers the cellular surface of *C. crescentus* by forming a 22 nm-repeat hexameric

55 crystal lattice and is non-covalently anchored to an ~18 nm thick LPS outer membrane[13–17]

56 (Figure 1a,b). The surface topology of stalked and predivisional *C. crescentus* includes a

57 cylindrical stalk measuring roughly 100 nm in diameter while the crescentoid cell body

58 approaches 800 nm in width[18,19] (Figure 1d). This large variety of curved topologies guarantees

59 that crystal distortion and defects within the S-layer lattice structure are present, defects which

60 enable complete coverage of the bacterial surface[4,13,20,21]. We can use Gaussian curvature, the

61 product of the maximum and minimum curvatures at a given point, to quantify the cellular

62 topology[22]. Crystalline defects cluster at regions with high absolute values of Gaussian curvature

63 such as the cell poles and division plane, while grain boundaries occur where Gaussian curvature

64 approaches zero such as the cell body (Figure 1d)[20,21].

65   Specifically labeling the S-layer *in vivo* has proven difficult due to the SLP's life cycle

66 and functions, which include secretion, refolding, anchoring, and crystallization[11,16,17,23,24].

67 Previously, electron microscopy of the *C. crescentus* S-layer was performed by inserting cysteine

68 residues into the RsaA sequence and labeling the protein with nanogold via maleimide

69 chemistry[13]. One such variant, henceforth referred to as CysRsaA, consists of a small tail added

70

3
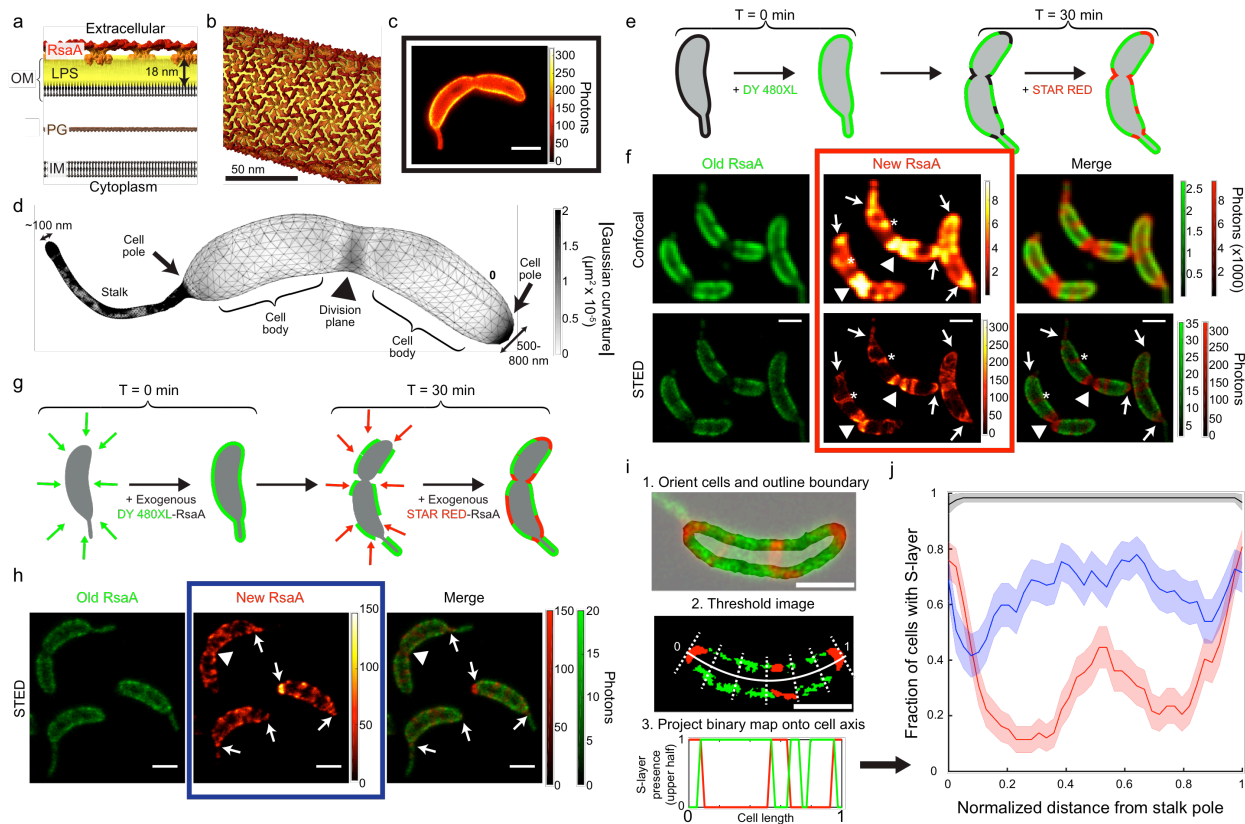
71

Figure 1. *Localized S-layer assembly occurs primarily at the poles and division plane, independent of secretion.* a) Schematic of the *C. crescentus* cell envelope with the S-layer crystal lattice (red/orange) anchored to the outer membrane (OM) via an 18 nm thick LPS layer (yellow), peptidoglycan (PG), and inner membrane (IM). b) Model of the RsaA S-layer structure (EMD-3604) applied to the surface of a 100 nm diameter cylinder. c) STED fluorescence microscopy image of a CysRsaA cell labeled with STAR RED. d) 3D mesh representation of predivisional *C. crescentus* topology with absolute value of Gaussian curvature projected onto the surface (gray shading). e) Schematic of 2-color pulse-chase experiment to image the sites of S-layer assembly where fluorophores DY-480XL and STAR RED were added to CysRsaA cells 30 min apart, washing in between. f) Confocal (top) and STED images (bottom) show localized assembly of natively produced S-layer at the cell poles (arrows), division plane (triangles), and crack-like features on the cell body (asterisks). g) Schematic of pulse-chase experiment where saturating quantities of purified, fluorescently labeled CysRsaA are added to the media of ΔRsaA cells. h) Endpoint STED images show localization of newly incorporated CysRsaA protein at the cell poles (arrows), division plane (triangle), and other locations. i) Overview of analysis method. Top: Cells were horizontally aligned with the stalk on the left side and the cell boundary was identified (non-gray region). Middle: S-layer was identified in both channels via intensity thresholding, and the binary image is projected along the normalized cell axis. Bottom: The projected image created two binary profiles of the S-layer for the upper and lower half of the cell in each color channel (red and green lines). j) S-layers produced natively (red, representative cell in red boxed image from Fig 1f) or by exogenous protein addition (blue, representative cell in blue boxed image from Fig 1h) show preferential incorporation at the cell poles and division plane, while control cells (black, representative cell in black boxed image from Fig 1c) show uniform labeling. Shaded regions show 95% confidence intervals for n=81, 75, and 57 cells for native, exogenous, and control cells, respectively. Scale bars = 1 μm except where noted.

4

72   to the N-terminus of RsaA, which includes a single cysteine residue[13] (Supp Fig. 1, Methods).

73   CysRsaA-producing cells divide normally and create a stable S-layer at a rate similar to that of

74   WT cells, and protein can be extracted and purified as a monomeric species (Supp Fig. 1).

75   Covalently modifying CysRsaA with membrane-impermeable fluorophores via

76   maleimide chemistry is a robust, highly specific labeling scheme for RsaA and enables live-cell

77   STimulated Emission Depletion (STED) fluorescence microscopy showing a complete S-layer

78   (Figure 1c; Supp Fig. 2). Pulse-chase STED imaging of living cells was performed using DY-

79   480XL as the pulse fluorophore and STAR RED as the chase with a 30 min delay (Figure 1e,f).

80   Using only stalked and predivisional cells oriented in the same direction, we found highly

81   localized S-layer assembly in growing cells characterized largely by new protein enrichment at

82   both cell poles and the division plane (Figure 1f,i,j; Supp Fig. 3), in agreement with observations

83   by electron microscopy[25]. However, high-efficiency labeling coupled with super-resolution

84   STED imaging revealed nano-scale crack-like features of new RsaA on the cell body, indicating

85   additional sites of localized S-layer assembly (Figure 1f).

86   We sought to determine the factors that contribute to S-layer assembly by examining how

87   RsaA secretion, cell wall growth, and the presence of an existing S-layer structure affect the

88   location of S-layer assembly in living cells. To determine whether RsaA secretion is necessary to

89   localize S-layer assembly, we added purified, fluorescently labeled CysRsaA to cultures of cells

90   with a genomic deletion of the *rsaA* gene (ΔRsaA). Saturating quantities (600 nM) of DY-480XL

91   labeled CysRsaA were introduced as a pulse, followed by a wash, 30 min of cell growth, and

92   another saturating quantity of STAR RED labeled CysRsaA as chase (Figure 1g). This

93   experiment revealed that exogenously added CysRsaA preferentially incorporates at the poles

94   and division plane (Figure 1h), in addition to increased incorporation along the cell body (Figure

5

95   1j, blue) compared to native S-layer assembly (Figure 1j, red). Previous immuno-gold staining

96   and electron microscopy of RsaF, the outermost component of the RsaA secretion apparatus,

97   indicated diffuse localization[23,26]. Therefore, localized S-layer assembly occurs independent of

98   RsaA secretion.

99   To investigate the effect of changing cell wall surface area on S-layer assembly, we

100   manipulated peptidoglycan insertion using the specific MreB perturbing compound, A22[27].

101   Under normal conditions, the cell wall grows mainly at the polar-proximal base of the stalk and

102   around the middle of the cell body, which eventually becomes the division plane[2]. These regions

103   alone are insufficient to explain localized S-layer assembly due to the additional appearance of

104   signal at the pole opposite the stalk (Figure 1j). At 2 μg/mL, A22 delocalizes MreB but still

105   allows some peptidoglycan addition along the cell body, leading to lemon-shaped cells that

106   divide slowly[27] (Supp Fig. 4). At 25 μg/mL, A22 fully inhibits peptidoglycan insertion and

107   surface area addition stops completely except at division planes where constriction began before

108   drug exposure[27] (Supp Fig. 4). Using a pulse-chase labeling scheme after drug treatment (Figure

109   2a), we found that cells treated with 2 μg/mL A22 maintain bipolar localized S-layer assembly,

110   but the amount of new RsaA incorporated along the cell body increased (compare red and green

111   highlighted columns in Figure 2b,c). At 25 μg/mL A22, bipolar localized S-layer assembly is

112   disrupted as evidenced by a decrease in signal at both poles (Figure 2b,c, black). If PG insertion

113   were the only driver of S-layer assembly, disruption should have occurred only at the stalked

114   pole, rather than both.

115   Treating cells with cephalexin prevents cell division by inhibiting peptidoglycan insertion

116   at the division plane[28] (Supp Fig. 5). In cephalexin-treated cells, S-layer assembly follows

117   untreated localization patterns, but with more crack-like features of new RsaA on the

118

6
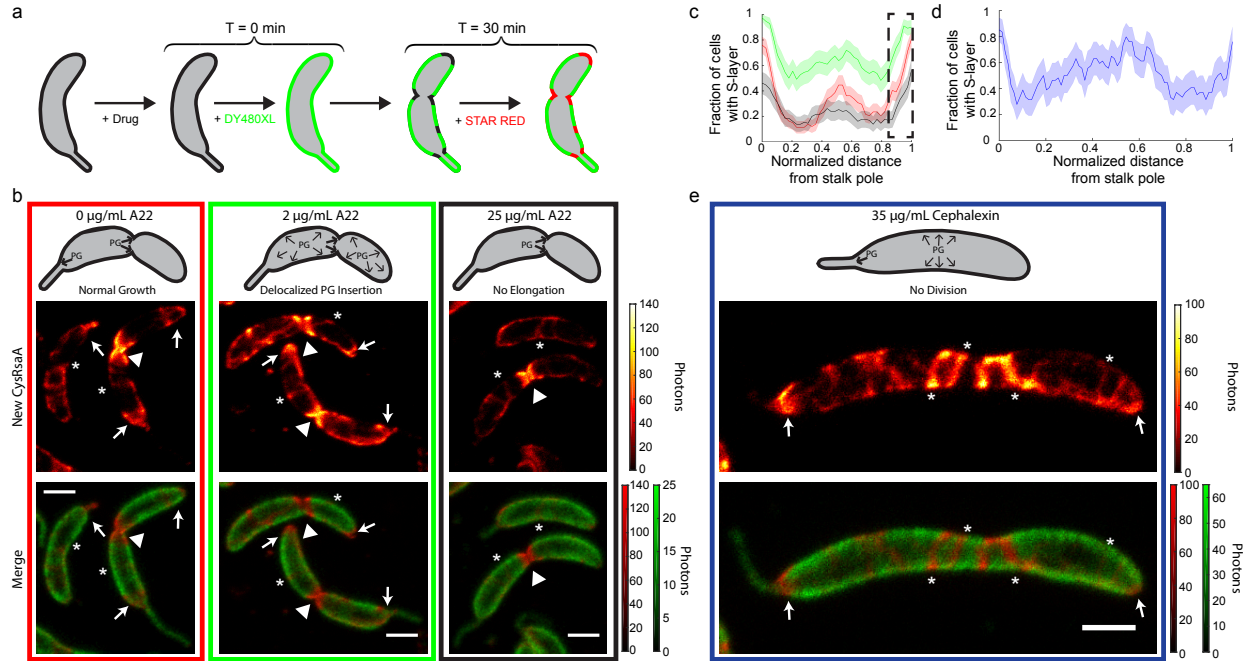
119

Figure 2. *S-layer assembly on the cell body spatially correlates with cell wall growth whereas assembly at the poles correlates with surface area production.* a) Schematic of pulse-chase labeling of CysRsaA cells treated with A22 (to inhibit MreB) for 1 hr or cephalexin (to inhibit cell division) for 3 hrs. b) Upper: Schematic showing effect of A22 treatment on PG insertion in *C. crescentus*, where untreated cells add PG primarily at the stalk pole and division plane, cells treated with 2 μg/mL A22 exhibit delocalized PG insertion along the entire cell with enrichment at the division plane, and cells treated with 25 μg/mL A22 have PG insertion exclusively at the division plane. Lower: STED images of S-layer assembly for treated cells with signal at the poles, division planes, and crack-like features marked by arrows, triangles, and asterisks, respectively. c) Quantitation of S-layer assembly localization on cells treated with 2 μg/mL A22 (green) show similar degrees of polar localization, but enhanced localization along the cell body compared to untreated cells (red curve; reproduced from Fig 1j). Polar localized S-layer assembly is decreased in cells treated with 25 μg/mL A22 (black), including the pole opposite the stalk (black dashed box). Shaded regions show 95% confidence intervals for n=81, 54, and 63 cells for 0 μg/mL, 2 μg/mL, and 25 μg/mL A22 treatment, respectively. d) Quantitation of S-layer assembly localization on cells treated with 35 μg/mL cephalexin show localization at both poles. Shaded region shows 95% confidence interval for n=25 cells. e) Upper: Schematic showing effect of 35 μg/mL cephalexin, which halts PG insertion during cell division. Bottom: STED image of CysRsaA cell treated with cephalexin shows localized S-layer assembly at both poles (arrows) while also adding S-layer at crack-like features (asterisks) along the cell body. Scale bars = 1 μm

7

120   significantly elongated cell body (Figure 2d,e). Taken together, both drug treatments show that

121   S-layer assembly on the cell body appears to correlate with localized cell wall growth while

122   bipolar localization is not driven by PG insertion alone.

123   Physically removing the S-layer from a CysRsaA cell provides a clean surface with

124   which to observe the cell replacing its own S-layer, which we term *de novo* assembly. Calcium

125   depletion (50 μM $CaCl_2$ instead of 500 μM $CaCl_2$ normally present in minimal growth medium)

126   has been shown to cause shedding of the RsaA S-layer[29,30]. Upon reintroducing 500 μM $CaCl_2$, a

127   new S-layer is produced on the surface of *C. crescentus* (Figure 3a). A time course of *de novo* S-

128   layer assembly using only one fluorophore label at different time points displays the appearance

129   of several S-layer patches per cell within an hour of calcium introduction (Figure 3b,c). By 2 hrs,

130   cells have produced a mostly complete S-layer, which agrees with the 2 hr doubling time of *C.*

131   *crescentus* (Figure 3c; Supp Fig. 6). Localization analysis of *de novo* S-layer assembly at 30 min

132   reveals its exclusion at the poles in sharp contrast to S-layer assembly in cells with a pre-existing

133   S-layer, which prefers the poles and division plane (red curve, Figure 3j).

134   To determine how these patches grew, we performed pulse-chase imaging of *de novo* S-

135   layer assembly (Figure 3d). This experiment revealed that initial S-layer patches expand from the

136   perimeter of each patch (Figure 3e), consistent with nucleation and growth characteristic of *in*

137   *vitro* SLP crystallization observed by time-resolved atomic force microscopy[10,31]. To further

138   evaluate this mode of assembly, very low concentrations (2.5 to 20 nM) of purified, STAR RED

139   labeled CysRsaA were added to cultures of ΔRsaA cells and puncta were observed (Figure 3f,g).

140   The number of puncta appeared dependent on CysRsaA concentration whereas the number of

141   molecules in each punctum did not positively correlate with CysRsaA concentration from 5 to 20

142   nM (Figure 3g,k). Adding 5 nM of exogenously purified and labeled DY-480XL CysRsaA
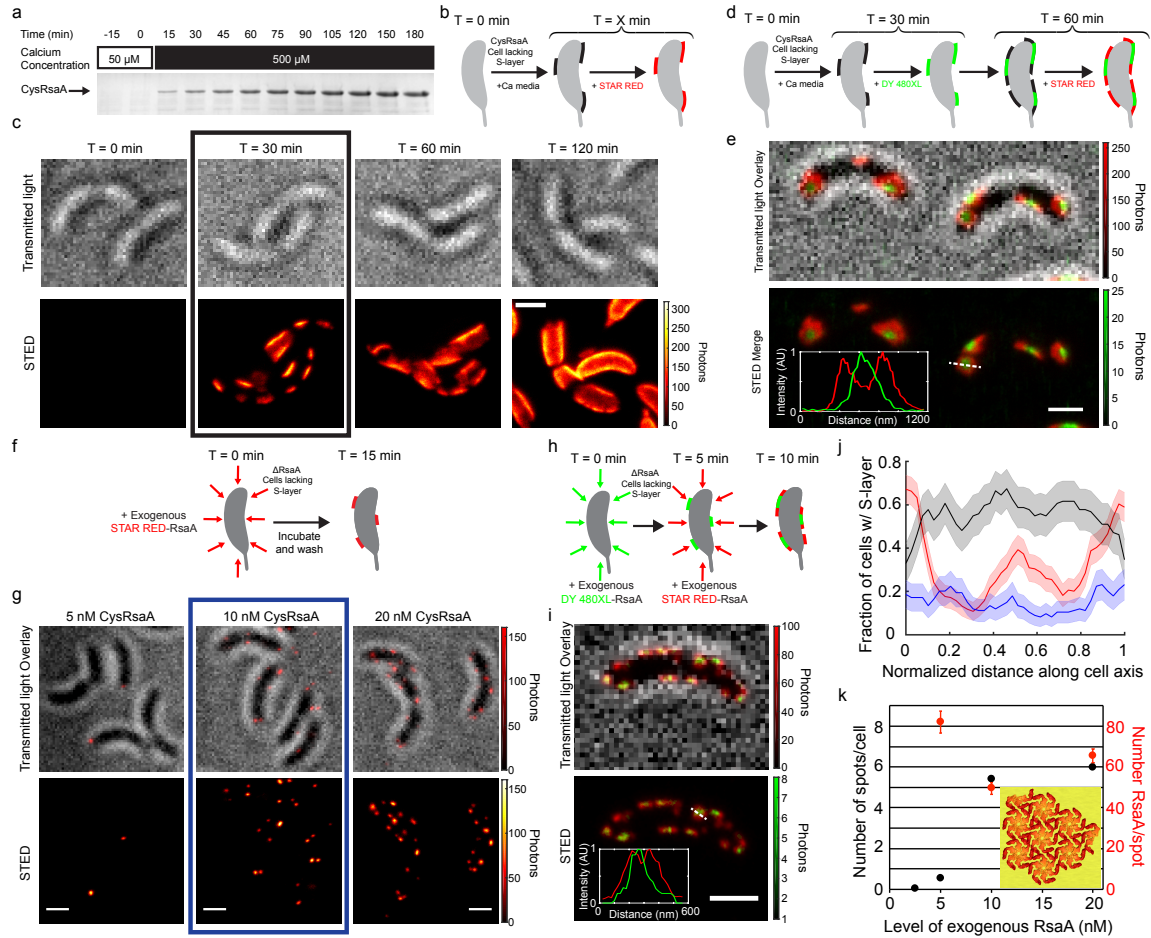
8

Figure 3. *In the absence of an existing S-layer structure, RsaA crystallizes on the cell surface with localization dependent on pre-existing crystal size.* a) Coomassie-stained SDS-PAGE of protein samples extracted from the surface of CysRsaA cells grown in low calcium M2G (50 μM $CaCl_2$, t<0 min) and then switched to 500 μM $CaCl_2$ (0 < t < 180 mins) show *de novo* accumulation of the S-layer. b) Schematic of *de novo* S-layer assembly experiment where CysRsaA cells are resuspended in M2G with 500 μM $CaCl_2$ and then their S-layer is labeled with STAR RED. c) A STED imaging time course of STAR RED labeled CysRsaA cells shows that *de novo* assembly of a new S-layer occurs at discrete patches that grow larger over time. d) Schematic of 2-color pulse-chase labeling between 30 and 60 minutes after calcium addition. e) STED imaging reveals growth of S-layer patches from their perimeter (red signal at the edges of green patch) and is confirmed by line profiles of the dashed line (inset). f) Schematic of experiment where low concentrations of STAR RED-labeled CysRsaA are incubated with ΔRsaA cells for 15 mins. g) STED images show exogenous CysRsaA nucleates small puncta of S-layer. h) Schematic of 2-color stepwise addition of 5 nM DY-480XL labeled CysRsaA followed by 10 nM STAR RED labeled CysRsaA. i) STED imaging shows that puncta on the cell surface formed by exogenous addition of purified CysRsaA grow from their perimeter, confirmed by line profiles of the dashed line (inset). j) Quantitation of S-layer assembly localization for native S-layer assembly (red), *de novo* native S-layer assembly (black), and S-layer assembly by exogenous addition of labeled CysRsaA (blue). Shaded regions show 95% confidence intervals for n=100, 50, and 65 cells for native, *de novo*, and exogenous protein addition, respectively. k) Quantitation of the number of S-layer puncta and average number of RsaA molecules per punctum on ΔRsaA cells upon addition of purified CysRsaA protein. A model of an RsaA crystal of about the measured size is shown (inset). Scale bars = 1 μm (panels c, e, g, i)

143

144   followed by 10 nM of STAR RED CysRsaA revealed expansion of fluorescent puncta from the

145   perimeter, as observed with two-color native *de novo* S-layer assembly (Figure 3e,h,i). These

146   observations are consistent with each punctum representing a nucleated RsaA protein crystal of

147   at least 7 RsaA hexamers (Figure 3k, inset). Large, natively grown S-layer crystals initially

148   exclude the cell poles (Figure 3c,j); however, introducing exogenously purified RsaA to ΔRsaA

149   cells creates small S-layer crystals that appear more uniformly distributed along the cell axis

150   (Figure 3j).

151   If *de novo* S-layer assembly occurs through nucleation and 2D crystallization of RsaA,

152   then protein self-assembly could also be responsible for continuous S-layer growth. Since protein

153   crystallization is concentration-dependent, we predict that once secreted, RsaA monomers should

154   be able to diffuse while non-covalently anchored to the LPS outer membrane until incorporated

155   into a nucleating or growing S-layer crystal. Indeed, at 1 nM exogenous CysRsaA, cells exhibit

156   weak diffuse fluorescence suggestive of diffusing molecules (Supp Fig. 7). Therefore, we

157   employed SMT to dynamically track the location of individual CysRsaA monomers anchored to

158   the LPS outer membrane. ΔRsaA cells were first pre-treated with 2.5 nM Cy3-CysRsaA to form

159   sparse, immobile S-layer crystalline patches or "seeds" on the LPS outer membrane (Figure 4a,

160   green). Then, 1 nM AlexaFluor647-CysRsaA (Figure 4a, red) was added to the growth media,

161   allowing single molecules to flow into the microscope's viewing area. Once attached to the LPS

162   outer membrane, CysRsaA molecules were imaged for several minutes at a time (Figure 4b).

163   CysRsaA tracks included entirely immobile molecules, entirely mobile molecules, and molecules

164   that appear to sample mobile and immobile states during the experiment (Figure 4b,c; Supp Fig.

165   8, 9). Correlating mobility of the molecule with distance measurements from a nearby S-layer

166   seed (Cy3 signal) reveals behavior consistent with binding at the edge of a growing S-layer
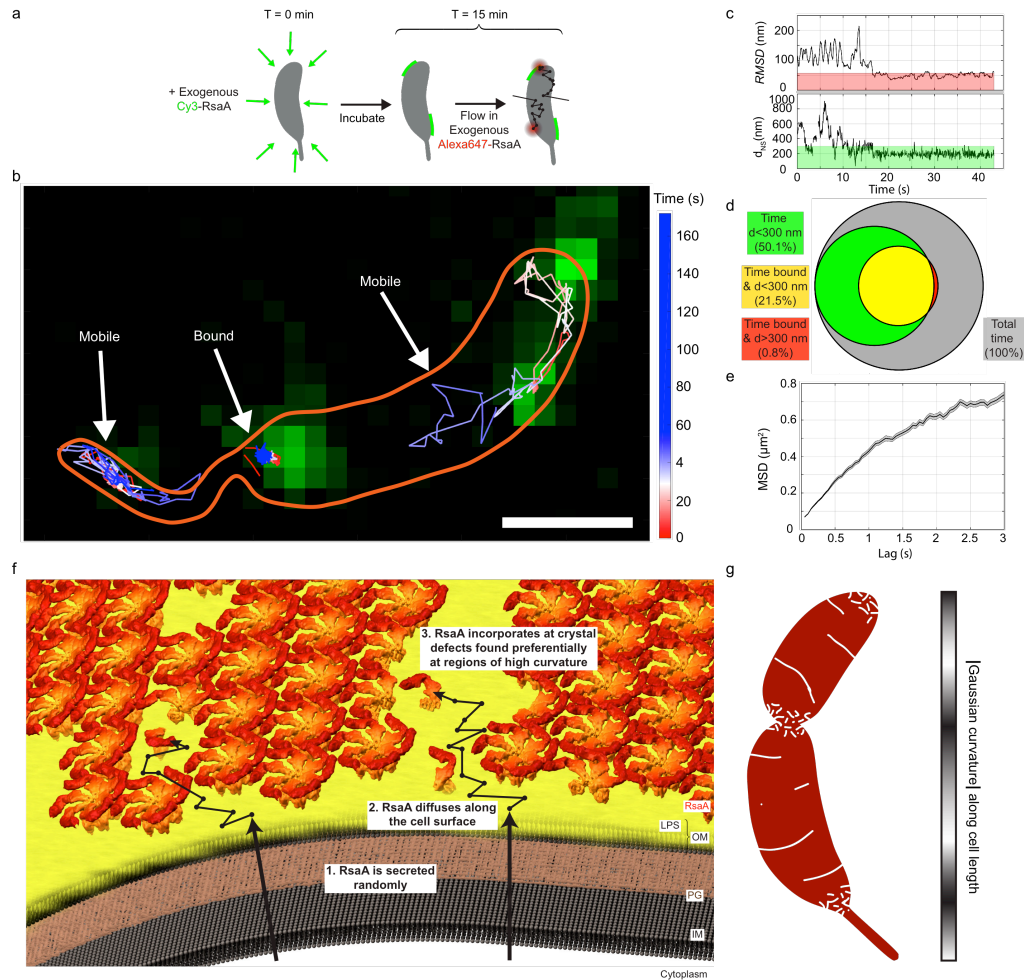
167

Figure 4. *RsaA monomers are mobile on the outer bacterial surface and bind to S-layer crystals.* a) Schematic of 2D, 2-color single-molecule tracking of CysRsaA on a ΔRsaA cell. Cells were incubated with 2.5 nM Cy3-labeled CysRsaA (green) to create small fluorescent seed crystals. Single molecules of AlexaFluor647 labeled CysRsaA diffused through the agarose mounting pad and bound to the cell surface. b) Single-molecule tracking (SMT) shows mobile and immobile single-molecule tracks. The cell boundary is sketched in orange. Scale bar = 1 μm. c) Upper: The RMSD from a nearby seed of an example track shows binding of the molecule from ~16-43s. Binding is defined as RMSD<57.3 nm (red shaded region). Lower: Distance from the nearest nucleation seed (d_{NS}) for the same track shows the molecule binds ~200 nm from the center of a crystal patch. Green shaded region shows the 300 nm threshold used for determining crystal patch proximity. d) A quantitative Venn diagram displaying the total time (grey area), and the fractions of time molecules spend near a crystal patch (green area), bound (yellow area), and bound but not near a crystal patch (red area), shows that when molecules cease diffusing, they are almost always in close proximity to an existing crystal patch. e) MSD analysis from 3D SMT of AlexaFluor647 labeled CysRsaA molecules revealing a diffusion coefficient of D = 0.077 μm^2/s. Shaded regions represent SEM. f) A generalizable model for S-layer assembly including secretion, diffusion, and incorporation at gaps within the S-layer lattice. g) A model for S-layer crystal boundaries/defects (white) mapped onto the *C. crescentus* surface (red), suggested by Gaussian curvature calculations (gray colorbar, right).

168

11

169   crystal (Figure 4c,d; Supp Fig. 9). Tracking CysRsaA anchored to the LPS outer membrane

170   while utilizing a double helix point-spread function for 3D localization[18] allowed calculation of

171   an apparent diffusion coefficient, D=0.077 μm^2/s (Figure 4e, Methods). A comparison with the

172   recent SMT of a similarly sized transmembrane signaling protein anchored to the inner

173   membrane of *C. crescentus*, CckA (D=0.0082 μm^2/s)[32], reveals that CysRsaA diffuses an order

174   of magnitude faster.

175   Based on these observations, we propose a model of S-layer assembly in *C. crescentus*

176   whereby RsaA monomers are secreted randomly and subsequently explore the LPS outer

177   membrane by diffusion until captured and incorporated into the growing crystalline S-layer

178   structure (Figure 4f). While SMT of RsaA was performed on ΔRsaA cells, it is plausible that

179   RsaA diffuses either on or within the LPS outer membrane, depending on whether an existing S-

180   layer structure is present above the site of RsaA secretion. Protein diffusion within the LPS outer

181   membrane in gram-negative bacteria has been observed by fluorescence recovery after

182   photobleaching, but individual LPS molecules are immobile[33]. In *C. crescentus*, the LPS outer

183   membrane is ~18 nm thick, while the size of a single RsaA monomer can be approximated by its

184   radius of gyration (Rg=5.8 nm)[14,30].

185   Our results imply that continuous S-layer crystallization occurs at gaps, defects, and grain

186   boundaries within the S-layer structure caused by localized cell wall growth or the inherent

187   topology of the cell surface (Figure 4g). Increasing localized cell wall growth along the cell body

188   (treatment with 2 μg/mL A22) increases S-layer assembly at that location; however, preventing

189   cell elongation (treatment with 25 μg/mL A22) disrupts S-layer assembly at both poles,

190   indicating that an additional factor is coordinating this process (Figure 2c)[2]. When the cell lacks

191   an existing S-layer and assembles a new one using a few large crystalline patches, S-layer

192   coverage initially excludes the poles rather than preferentially assembling there (Figure 3j).

193   Decreasing the size of nucleated S-layer crystals by adding exogenous RsaA to ΔRsaA cells

194   disrupts polar exclusion (Figure 3j), indicating that an underlying tether within the LPS is not

195   responsible for localizing S-layer assembly.

196   The molecular defects and boundaries created by imposing a large crystalline lattice on a

197   variably curved surface are sufficient to explain these observations[20,21]. Regions of non-zero

198   Gaussian curvature values on a 3D model of the *C. crescentus* topology correlate with the polar

199   and divisional regions of S-layer assembly observed in this study (Figure 1d,j, 4g). At these

200   regions, we expect small crystalline patches with more defects, allowing for more local RsaA

201   incorporation. Along the cell body, changes in curvature are less dramatic, which produce longer

202   grain boundaries between large crystalline patches[20,21]. The crack-like features of new RsaA we

203   observe on the cell body further support the model that S-layer assembly patterning reflects

204   growth at natural imperfections in the S-layer crystalline lattice (Figure 1f, 2b,e).

205   In *C. crescentus*, RsaA deletion and the subsequent loss of an S-layer disrupts normal cell

206   growth, suggesting a connection between the S-layer structure and cellular fitness[30]. Given the

207   central role of RsaA crystallization in S-layer assembly and this connection to fitness, the

208   protein's ability to self-assemble may drive natural selection of the RsaA amino acid sequence.

209   Remarkably small but stable RsaA protein crystals consist of only ~50 molecules (Figure 3g,k),

210   suggesting that efficient nucleation at low concentrations may be another selectable trait

211   supporting protein self-assembly. SLPs are exceptionally diverse in sequence, varying widely in

212   size (40-200 kDa) and fold[4]. Functional convergence of diverse crystalline structures can be

213   rationalized by selection driven by protein self-assembly, which can occur independently of

214   overall fold and instead requires just a few key surface residues making symmetric, planar

13

215 crystal contacts[34,35]. Similarly, diverse SLPs in archaea prefer charged (acidic or basic) amino

216 acids to facilitate nutrient uptake through the nanoporous S-layer—a function that evolves

217 independently of protein fold[36].

218   The mechanisms by which bacteria build, maintain, and evolve their S-layers are

219 important to human health and our ability to treat and respond to bacterial pathogens such as *C.*

220 *difficile, A. salmonicida,* and *B. anthracis*[37–39]. Additionally, S-layers have been exploited as

221 nanomaterials in a variety of applications[4,40], including high-density organization and display of

222 organic or inorganic molecules tethered to RsaA in particular[41,42]. This study proposes a

223 mechanism by which bacteria can control extracellular structures without direct intracellular

224 feedback, exploiting the biophysics of macromolecular 2D crystalline self-assembly on curved

225 3D surfaces. In particular, defects and natural imperfections within the S-layer lattice serve as

226 sites of new S-layer growth. Further manipulation of this seemingly unsupervised assembly

227 pathway may lead to treatments that target cell surface structures such as the S-layer or allow

228 enhanced utilization of S-layers as self-assembling macromolecular nanomaterials.

229

230 Materials and Methods

231 **Strains**

232   Three strains were used in this study and are available from the corresponding author

233 S.W. upon request. *C. crescentus* NA1000*,* which is referred to as wild type (WT) throughout the

234 text, was used as a control for fluorescent labeling, S-layer protein production, and drug

235 treatment response. An RsaA-negative strain of NA1000, referred to as ΔRsaA, was generated

236 via clean genomic deletion. We amplified 802 bp upstream and 806 bp downstream of *rsaA*

237 using   primer   pairs   RsaAUpstreamF/R   (5'-

14

238   CTACGTAATACGACTCAGGCCGCGATCAGTGCCGACGCG-3'   and   5'-

239   ACGTTCGCTTAGGCCATGAGGATTGTCTCCCAAAAAAAATCCCACACCC-3')   and

240   RsaADownstreamF/R   (5'-TGGCCTAAGCGAACGTCTGATCCTCGCCTAG-3'   and   5'-

241   CGGCCGAAGCTAGCGGGCCATGGTGGCCATCTGGATC-3'). The two fragments were

242   inserted into SpeI and EcoRI-linearized pNPTS138 by Gibson assembly. The resulting plasmid

243   was electroporated into *C. crescentus* NA1000. Deletion mutant was isolated using a two-round

244   selection approach[43].

245   For fluorescence microscopy and protein purification, a cysteine mutant of RsaA,

246   CysRsaA, was created as previously described[13]. Briefly, RsaA with a 7-residue N-terminal tail

247   was cloned into the p4A vector and introduced to background strain JS1023 by

248   electroporation[13,17]. JS1023 contains the repBAC operon to enable plasmid replication as well as

249   an amber mutation within the native *rsaA* gene and a disruptive insertion within the gene for an

250   S-layer associated protease, *sap*[17].

251   **S-layer Protein Purification**

252   Purified RsaA in the absence of $CaCl_2$ was previously shown to partially unfold at

253   28°C[30]. Therefore, CysRsaA samples were kept cold (<4°C) at all times unless otherwise noted.

254   CysRsaA protein was purified similarly to previously reported methods[30,44]. CysRsaA-producing

255   *C. crescentus* cells were grown to early stationary phase at 30°C in PYE medium, shaking at 200

256   rpm. The culture was then pelleted by centrifugation and stored at -80°C. Approximately 1 g of

257   cell pellet was thawed on ice, re-suspended with 10 mL of ice cold 10 mM HEPES buffer pH

258   7.0, and centrifuged for 4 min at 18,000 rcf. This washing step was performed three times. The

259   pellet was then separated into 10 aliquots and 600 μL of 100mM HEPES buffer pH 2.0 was

260   added to each aliquot. These cell suspensions were incubated on ice for 15 min and then spun for

15

261   4 min at 18,000 rcf. The supernatants were then pooled and neutralized (pH = 7) by the addition

262   of 5 N NaOH. To remove free divalent cations and reduce cysteine side chains, 5 mM

263   Ethylenediaminetetraacetic acid (EDTA) and 1 mM Tris(2-carboxyethyl)phosphine

264   hydrochloride (TCEP) were added. The protein solution was then syringe filtered using a 0.22

265   μm PES syringe filter and 5 mL were injected onto a Highload Superdex200 16/600 size

266   exclusion column (GE Healthcare). During size exclusion chromatography, the running buffer

267   consisted of 50 mM Tris/HCl pH 8.0 and 150 mM NaCl. Monomeric CysRsaA consistently

268   eluted at approximately 0.55 column volumes (Supp Fig. 1). From 1 g of pelleted cells, we

269   consistently purified at least 1 mg of monomeric CysRsaA protein. Purity was assessed by SDS-

270   PAGE (Supp Fig. 1).

271   **Time-resolved Blot**

272   WT or CysRsaA-producing *C. crescentus* cells were grown in modified M2G medium

273   containing 50 μM $CaCl_2$ (normally 500 μM) to log phase (OD_{600nm} = 0.5). At t=0 min, $CaCl_2$

274   was adjusted to 500 μM using a sterile 1 M stock. The culture was then incubated at 30°C,

275   shaking at 180 rpm with 0.5 mL aliquots removed every 15 minutes. Aliquots were immediately

276   spun down and snap frozen in LN_2. Soluble RsaA extraction was performed as above (without

277   chromatography) and analyzed by SDS-PAGE.

278   **Fluorescent Labeling of the S-layer Protein**

279   CysRsaA protein was fluorescently labeled by covalent maleimide chemistry both *in vivo*

280   and *in vitro*. For *in vivo* experiments, 1 μM STAR RED (Abberior) or DY-480XL (Dyomics)

281   Cys-reactive fluorescent label was introduced to 1 mL of log-phase ($0.1 < OD_{600nm} < 1.0$) CysRsaA

282   cells in minimal medium (M2G) at 30°C. After 15 minutes, cells were washed with 1 mL of

283   M2G once if another fluorophore was to be added next or twice if the next step was imaging.

16

284   Complete labeling was evidenced by highly spatially complementary fluorescent images in

285   pulse-chase labeled cells (Fig. 1b).

286   For *in vitro* experiments, purified CysRsaA was buffer exchanged into 50 mM HEPES

287   pH 7.0 and 150 mM NaCl using a 30 kDa MWCO centrifugal concentrator (Sartorius).

288   Overnight labeling of CysRsaA protein (>20 μM) was performed on ice with the addition of 1

289   mM TCEP and at least 5-fold stoichiometric excess of maleimide-derivatized STAR RED, DY-

290   480XL, Cy3 (Lumiprobe), or AlexaFluor647 (ThermoFisher). The next day, three successive

291   1:30 dilutions were performed to remove unbound dye molecules using a 30 kDa MWCO

292   centrifugal concentrator (Sartorius) and buffer containing 50 mM Tris/HCl pH 8.0 and 150 mM

293   NaCl. Absorbance measurements at 280 nm and the known absorbance peak for each

294   fluorophore determined labeling efficiency, which varied from 50-90%.

295   **Growth Curves**

296   For growth curve analysis of WT and ΔRsaA *C. crescentus* strains, 10 μL of mid-log

297   phase cultures (OD_{600nm}=0.5) were added to 90 μL of M2G containing varying amounts of A22

298   (Cayman Chemical) or cephalexin (Frontier Scientific) in a sterile, black-walled, 96-well

299   transparent plate (Corning). While incubating the plate at 29°C and shaking at 600 rpm between

300   readings, OD_{600nm} was measured every 5 minutes for up to 23 hours using an Infinite M1000

301   microplate reader (Tecan).

302   **Confocal and STED Microscopy**

303   Images were acquired on a bespoke 2-color fast scanning STED microscope described

304   previously[22]. Briefly, the pulsed 750 nm depletion beam is provided by a titanium-sapphire

305   mode-locked oscillator (Mira 900D, Coherent) running at 80 MHz, providing an average power

306   of 120-130 MW/cm^2 at the sample plane. A vortex phase plate imparts the STED donut shape

17

307   (RPC Photonics). 530 nm and 635 nm pulsed diode lasers are used for excitation (LDH-P-FA-

308   530B & LDH-P-C-635B, PicoQuant), providing an average power of 40-60 kW/cm^2 and 50-80

309   kW/cm^2, respectively. The laser beams are focused and fluorescence is collected through an oil

310   immersion objective (Plan Fluor 100x/1.3 NA, Nikon). A 7.5 kHz resonant mirror (Electro-

311   Optical) scans the beams along the fast axis, while the slow axis is scanned using a piezo stage

312   (PD1375, Mad City Labs). Fluorescence is collected through a ~0.7 Airy unit (AU) and 0.8 AU

313   pinhole (red and green channels, respectively), spectrally filtered from 650-710 nm or 550-615

314   nm, and detected on a Si APD detector (SPCM-ARQH-13, Perkin Elmer). Microscope control

315   and image acquisition arose from a custom LabView program running on an FPGA (PCIe-

316   7842R, National Instruments). Confocal images are taken using no depletion laser, a pixel size

317   of 100 nm, and an average pixel dwell time of ~0.25 ms/pixel. STED images have a pixel size of

318   20 nm, and an average pixel dwell time of 0.1 ms/pixel for the red channel. Images in the green

319   channel are the sum of two frames, smoothed with a $\sigma = 0.9$ pixel Gaussian filter and an average

320   pixel dwell time of 30 µs/pixel/frame.

321   **Binary Cell Profile Analysis**

322   S-layer cell profiles were analyzed using a custom MATLAB algorithm (Supp Fig. 3).

323   STED images were aligned to the gradient of the transmitted light image via cross-correlation to

324   correct for sample drift during scanning. Well-separated cells were selected by hand and aligned

325   to be horizontal with the stalk on the left side using a radon transform (except Fig 3j, where

326   stalks cannot easily be identified on cells for *de novo* assembly and exogenous addition

327   experiments). A cell axis was determined by fitting a second order polynomial to the maximum

328   intensity transmitted light pixels. For the cephalexin treated cells, a smoothing spline was used

329   instead of a second order polynomial due to the longer cell length. Cells were classified as

18

330   swarmer or stalked, and swarmer cells were omitted from analysis. For each cell, a 200 nm wide

331   cell outline was defined. For conditions with a mostly complete S-layer (Fig 1d and 2c), first the

332   outer cell boundary was determined by thresholding a normalized sum of the two-color channels,

333   and then this outer boundary was eroded to form the 200 nm cell outline. For analysis including

334   conditions with an incomplete S-layer (Fig 3e), the center of the cell outline was determined by

335   finding the maximum gradient of the transmitted light image around the cell axis, followed by

336   expansion to a 200 nm wide cell outline. Then, the presence of S-layer was determined by

337   applying a binary intensity threshold to the STED images smoothed using a Gaussian filter with

338   σ=0.9 pixels (18 nm). An upper and lower binary cell profile were determined by projecting each

339   pixel onto the cell backbone and binning into 40 equi-length bins, where a single pixel identified

340   as positive for S-layer in a bin makes the entire bin positive. The fraction of cells with S-layer at

341   each position along the normalized cell axis can then be computed (combining both upper and

342   lower halves), yielding a binomial observation for the probability of finding S-layer at a given

343   position, $\hat{p}(x)$. 95% confidence intervals were determined using the Wilson score interval. All

344   imaging experiments except for Figures 2e, 3e, and 3i were performed on cell populations from

345   at least two independently created samples.

346   **Puncta Quantification**

347   Counting the number of crystal puncta per cell upon exogenous addition of RsaA was

348   performed by identifying spots with signal greater than 10 standard deviations above

349   background. Quantitation of the number of RsaA monomers per punctum was performed using a

350   custom MATLAB algorithm. In-focus puncta were fit using non-linear least squares to an

351   asymmetric Gaussian. These fits were used to determine the number of photons per punctum.

352   The number of photons per RsaA monomer was determined by imaging single molecules of

19

353   RsaA-STAR RED *in vitro* on a poly-L-lysine coated coverslip. By calculating the photons per

354   molecule of both STED and confocal images of the *in vitro* sample, a photobleaching correction

355   factor was determined by comparing the number of molecules identified in both confocal and

356   STED images of identical fields-of-view. The final number of RsaA monomers per punctum was

357   corrected for photobleaching as well as the *in vitro* labeling efficiency of the exogenously added

358   RsaA, as determined by absorbance at 280 nm and the absorbance of STAR RED at 640 nm.

359   **2D & 3D Single-Particle Tracking Microscopy**

360   Images were acquired on a custom-built 2-color inverted microscope (Olympus, IX71)

361   for imaging cy3 and AlexaFluor647 (Supp Fig 10). Labeled biological samples were mounted on

362   a 2D micrometer stage and in contact with an oil-immersion objective (Olympus, 100x, 1.4 NA,

363   UPLANSAPO). Shutters were used in a sequential, interleaved fashion, where the sample was

364   first exposed to the 641 nm laser (Coherent Cube, 100 mW) for 1.8 s at an intensity of 88.5

365   W/cm^2, then the 514 nm laser (Coherent Sapphire, 100 mW) for 0.2 s at an intensity of 1.6

366   W/cm^2. Emission is collected with the objective, passes through a dichroic filter (Semrock,

367   FF425/532/656-Di01), and another dichroic filter (594LP), which allows us to spectrally separate

368   the emission. Alexa647 emission is detected on one EMCCD camera (Andor, DU-897U-CS0-

369   #BV) with two emission filters (Chroma, 680-60; Chroma, 655LP) and Cy3 is detected on a

370   separate EMCCD camera (Andor, DU-897U-CS0-#BV) with an emission filter (Semrock, 578-

371   105), both recorded at a framerate of 20 frames/s and an electron-multiplying gain of 200.

372   During the first ~10 seconds of acquisition, the intensity of the 641 nm laser is briefly increased

373   to a higher intensity to allow the fluorescent dyes to bleach down approximately to the single-

374   molecule regime before reducing the intensity for optimal tracking. Spatial correlation between

375   the two cameras is determined by detecting Tetraspeck beads (Invitrogen), which appear in both

20

376   channels. 3D tracking was performed with a double-helix phase mask placed at the Fourier plane

377   in the detection side of our microscope. Imaging conditions are similar to our 2D single-particle

378   tracking experiments, except the 641nm laser was used for detecting labeled RsaA molecules

379   with an intensity of 885 W/cm^2. All image acquisition was performed through software made by

380   Andor. Pixel size is 163 nm. All tracks shown (Figure 4b and Supp Fig. 9) are down-sampled 5X

381   for clarity.

382   **3D Calibration with Fiducials**

383   In 3D single-molecule tracking, the double helix point spread function (DH-PSF) allowed

384   extraction of the *xyz* position of individual emitters in the field of view[45]. Spatial calibrations

385   utilized fluorescent beads (FluoSpheres 0.2 µm, crimson fluorescent (625/645)), spin-coated

386   from 1% polyvinyl alcohol onto a glass coverslip. Using a piezo-electric z-motion stage,

387   calibrations were acquired over a 3 µm range along the *z* axis with a 50 *nm* step-size with 30

388   frames measured at each *z*-height. This calibration step produces template images of the DH-

389   PSF, which are used for the identification of single-molecule signals during post-processing of

390   the raw data. All imaging was performed at 25°C. Using the *easyDHPSF* MATLAB program[46], a

391   *z*-axis calibration over a 3-*µm* range is obtained *via* a 2D Double-Gaussian fit, which provides us

392   with *xy* positions, width, amplitudes, and offset levels of each lobe of the fluorescent bead.

393   **Mobility Analysis of 2D RsaA Tracking Data**

394   Images of single molecules and beads were analyzed using custom-built MATLAB code.

395   Within one *C. crescentus* cell, a 2D symmetric Gaussian fit is applied to a single labeled RsaA

396   molecule of interest, which provides an estimate of its *xy* position at that point in time. Linking

397   together the trajectory of the same molecule over time generates tracks. In order to determine

398   whether the detected molecules were bound or not, we first calculated the root mean squared

399   deviation (RMSD) from the mean position over a 1 s sliding window (20 frames). Bound

400   molecules will have a relatively low RMSD (near the localization precision) compared to a

401   molecule freely diffusing within the cell. By performing this for every track (9 tracks) within the

402   same cell, we were able to generate a histogram of all RMSD values (6625 RMSD values),

403   which shows a clear peak with a tail (Supp Fig. 8), where the left-most peak arises from the

404   localization precision error for bound molecules. The Gaussian fit of the lowest RMSD

405   population was utilized to determine a binding threshold (RMSD < 57.3 nm) corresponding to

406   2σ above the mean. Molecules were classified as bound if RMSD < Threshold or unbound if

407   RMSD $\geq$ Threshold).

2-Color Analysis of 2D RsaA/Nucleation Site Tracking Data

409   The *xy* location of each nucleation site, labeled with Cy3, was separately determined by

410   fitting a 2D symmetric Gaussian. The locations of these nucleation sites was found to be

411   stationary over the ~15 minute imaging period. Using the 2D RsaA trajectories analyzed earlier,

412   we calculated the d_{NS}, which is defined as the distance between the RsaA molecule and the

413   nearest nucleation site. By calculating both the RMSD and the d_{NS}, we can categorize each frame

414   as the following: (a) bound only, (b) bound and close to a nucleation site, or (c) close to a

415   nucleation site only.

3D Mean Square Displacement (MSD) Analysis

417   Images of RsaA imaged in 3D were analyzed using custom-built MATLAB code for

418   analyzing DH-PSF data. A 2D Double-Gaussian fit was applied to each emitter in the field-of-

419   view, which provides us with x, y, and θ information from the tilt of the two lobes of the double-

420   helix. We use the calibration obtained earlier to convert our estimates to *xyz* values. For each

421   individual track, the MSD is computed over a series of time lags starting from 50 ms. We then

22

422   pool the data over all 30 trajectories to obtain a 3D MSD plot. The diffusion coefficient is

423   extracted by fitting the following equation to the first 4 time lags:

$$MSD_{3D} = 6D\left(\tau - \left(\frac{\tau_E}{3}\right)\right) + 2(s_1^2 + s_2^2 + s_3^2)$$

424   where D is the diffusion coefficient, τ is the time lag, τ_E is the exposure time of the camera (50

425   ms), and s_i is the localization error in the ith dimension ($s_{x,y,z}$ = 93 nm, 93 nm, 91 nm).

426   **Gaussian Curvature Analysis**

427   Point cloud localization data of positions on the *C. crescentus* surface were obtained

428   previously by a covalently surface-attached fluorophore[18]. A surface mesh was extracted with the

429   Poisson Surface Reconstruction algorithm, available through MeshLab, an open source software

430   package[47]. Gaussian curvature analysis was performed as previously described[22].

431   **Code Availability**

432   The code used in this study is either open access[46,47] or is described above and available

433   upon request.

434

435

436   References

437   1.   Figge, R. M., Divakaruni, A. V. & Gober, J. W. MreB, the Cell Shape-determining

438   Bacterial Actin Homologue, Co-ordinates Cell Wall Morphogenesis in *Caulobacter*

439   *crescentus*. *Mol. Microbiol.* **51,** 1321–1332 (2004).

440   2.   Aaron, M. *et al.* The Tubulin Homologue FtsZ Contributes to Cell Elongation by Guiding

441   Cell Wall Precursor Synthesis in *Caulobacter crescentus*. *Mol. Microbiol.* **64,** 938–952

442   (2007).

443   3.   Egan, A. J. F., Cleverley, R. M., Peters, K., Lewis, R. J. & Vollmer, W. Regulation of

444   Bacterial Cell Wall Growth. *FEBS J.* **284,** 851–867 (2017).

445 4. Sleytr, U. B., Schuster, B., Egelseer, E. M. & Pum, D. S-layers: Principles and

446   Applications. *FEMS Microbiol. Rev.* **38,** 823–64 (2014).

447 5. Albers, S.-V. & Meyer, B. H. The Archaeal Cell Envelope. *Nat. Rev. Microbiol.* **9,** 414–

448   426 (2011).

449 6. Zhu, C. *et al.* Diversity in S-layers. *Prog. Biophys. Mol. Biol.* **123,** 1–15 (2017).

450 7. Lau, J. H. Y., Nomellini, J. F. & Smit, J. Analysis of High-level S-layer Protein Secretion

451   in *Caulobacter crescentus*. *Can. J. Microbiol* **56,** 501–514 (2010).

452 8. Pum, D., Toca-Herrera, J. L. & Sleytr, U. B. S-Layer Protein Self-Assembly. *Int. J. Mol.*

453   *Sci.* **14,** 2484–2501 (2013).

454 9. Baranova, E. *et al.* SbsB Structure and Lattice Reconstruction Unveil Ca2+ Triggered S-

455   layer Assembly. *Nature* **487,** 119–122 (2012).

456 10. Chung, S., Shin, S.-H., Bertozzi, C. R. & De Yoreo, J. J. Self-catalyzed Growth of S

457   layers via an Amorphous-to-Crystalline Transition Limited by Folding Kinetics. *Proc.*

458   *Natl. Acad. Sci. U. S. A.* **107,** 16536–41 (2010).

459 11. Nomellini, J. F., Kupcu, S., Sleytr, U. B. & Smit, J. Factors Controlling *In Vitro*

460   Recrystallization of the *Caulobacter crescentus* Paracrystalline S-Layer. *J. Bacteriol.* **179,**

461   6349–6354 (1997).

462 12. Rad, B. *et al.* Ion-specific Control of the Self-Assembly Dynamics of a Nanostructured

463   Protein Lattice. *ACS Nano* **9,** 180–190 (2015).

464 13. Amat, F. *et al.* Analysis of the Intact Surface Layer of *Caulobacter crescentus* by Cryo-

465   electron Tomography. *J. Bacteriol.* **192,** 5855–65 (2010).

466 14. Bharat, T. A. M. *et al.* Structure of the hexagonal surface layer on *Caulobacter crescentus*

467   cells. *Nat. Microbiol.* **2,** 1–6 (2017).

468 15. Jones, M. D., Vinogradov, E., Nomellini, J. F. & Smit, J. The Core and O-Polysaccharide

469   Structure of the *Caulobacter crescentus* Lipopolysaccharide. *Carbohydr. Res.* **402,** 111–

470   117 (2015).

471 16. Bingle, W. H., Nomellini, J. F. & Smit, J. Linker Mutagenesis of the *Caulobacter*

472   *crescentus* S-Layer Protein: Toward a Definition of an N-Terminal Anchoring Region and

473   a C-Terminal Secretion Signal and the Potential for Heterologous Protein Secretion. *J.*

474   *Bacteriol.* **179,** 601–611 (1997).

475 17. Ford, M. J., Nomellini, J. F. & Smit, J. S-Layer Anchoring and Localization of an S-

476   Layer-Associated Protease in *Caulobacter crescentus*. *J. Bacteriol.* **189,** 2226–2237

477   (2007).

478 18. Lee, M. K., Rai, P., Williams, J., Twieg, R. J. & Moerner, W. E. Small-molecule Labeling

479   of Live Cell Surfaces for Three-dimensional Super-resolution Microscopy. *J. Am. Chem.*

480   *Soc.* **136,** 14003–14006 (2014).

481 19. Schredl, A. T., Perez Mora, Y. G., Herrera, A., Cuajungco, M. P. & Murray, S. R. The

482   *Caulobacter crescentus* ctrA P1 Promoter is Essential for the Coordination of Cell Cycle

483   Events that Prevent the Overinitiation of DNA Replication. *Microbiol. (United Kingdom)*

484   **158,** 2492–2503 (2012).

485 20. Garcia, N. A., Register, R. A., Vega, D. A. & Gómez, L. R. Crystallization Dynamics on

486   Curved Surfaces. *Phys. Rev. E* **88,** 12306 (2013).

487 21. García, N. A., Pezzutti, A. D., Register, R. A., Vega, D. A. & Gómez, L. R. Defect

488   formation and coarsening in hexagonal 2D curved crystals. *Soft Matter* **11,** 898–907

489   (2015).

490   22.   Yoon, J. *et al.* Revealing the Nanoscale Morphology of the Primary Cilium using Super-

491   resolution Fluorescence Microscopy. *Biophys. J.* **116,** 1–11 (2019).

492   23.   Awram, P. & Smit, J. The *Caulobacter crescentus* Paracrystalline S-layer Protein is

493   Secreted by an ABC Transporter (Type I) Secretion Apparatus. *J. Bacteriol.* **180,** 3062–9

494   (1998).

495   24.   Sotomayor-Pérez, A.-C., Ladant, D. & Chenal, A. Disorder-to-Order Transition in the

496   CyaA Toxin RTX Domain: Implications for Toxin Secretion. *Toxins (Basel).* **7,** 1–20

497   (2014).

498   25.   Smit, J. & Agabian, N. Cell Surface Patterning and Morphogenesis: Biogenesis of a

499   Periodic Surface Array During *Caulobacter* Development. *J. Cell Biol.* **95,** 41–49 (1982).

500   26.   Toporowski, M. C., Nomellini, J. F., Awram, P. & Smit, J. Two Outer Membrane Proteins

501   Are Required for Maximal Type I Secretion of the *Caulobacter crescentus* S-Layer

502   Protein. *J. Bacteriol.* **186,** 8000–8009 (2004).

503   27.   Gitai, Z., Dye, N. A., Reisenauer, A., Wachi, M. & Shapiro, L. MreB Actin-mediated

504   Segregation of a Specific Region of a Bacterial Chromosome. *Cell* **120,** 329–341 (2005).

505   28.   Chen, Y. E. *et al.* Spatial Gradient of Protein Phosphorylation Underlies Replicative

506   Asymmetry in a Bacterium. *Proc. Natl. Acad. Sci.* **108,** 1052–1057 (2011).

507   29.   Walker, S. G., Karunaratne, D. N., Ravenscroft, N. & Smit, J. Characterization of Mutants

508   of *Caulobacter crescentus* Defective in Surface Attachment of the Paracrystalline Surface

509   Layer. *J. Bacteriol.* **176,** 6312–6323 (1994).

510   30.   Herrmann, J. *et al.* Environmental Calcium Controls Alternate Physical States of the

511   *Caulobacter* Surface Layer. *Biophys. J.* **112,** 1841–1851 (2017).

512   31.   Stel, B., Cometto, F., Rad, B., De Yoreo, J. J. & Lingenfelder, M. Dynamically resolved

513   self-assembly of S-layer proteins on solid surfaces. *Chem. Commun.* **54,** 10264–10267

514   (2018).

515   32.   Lasker, K. *et al.* Phospho-signal flow from a pole-localized microdomain spatially

516   patterns transcription factor activity. *bioRxiv* 220293 (2018). doi:10.1101/220293

517   33.   Ghosh, A. S. & Young, K. D. Helical Disposition of Proteins and Lipopolysaccharide in

518   the Outer Membrane of *Escherichia coli*. *J. Bacteriol.* **187,** 1913–1922 (2005).

519   34.   Garcia-Seisdedos, H., Empereur-Mot, C., Elad, N. & Levy, E. D. Proteins Evolve on the

520   Edge of Supramolecular Self-assembly. *Nature* **548,** 244–247 (2017).

521   35.   Suzuki, Y. *et al.* Self-assembly of Coherently Dynamic, Auxetic, Two-dimensional

522   Protein Crystals. *Nature* **533,** 369–373 (2016).

523   36.   Li, P.-N. *et al.* Nutrient Transport Suggests an Evolutionary Basis for Charged Archaeal

524   Surface Layer Proteins. *ISME J.* **12,** 2389–2402 (2018).

525   37.   Kirk, J. A., Banerji, O. & Fagan, R. P. Characteristics of the *Clostridium difficile* Cell

526   Envelope and its Importance in Therapeutics. *Microb. Biotechnol.* **10,** 76–90 (2017).

527   38.   Garduno, R. A. *et al.* Host Cell Invasion and Intracellular Residence by *Aeromonas*

528   *salmonicida*: Role of the S-layer. *Can. J. Microbiol* **46,** 660–668 (2000).

529   39.   Kern, J. & Schneewind, O. BslA, the S-layer Adhesin of *Bacillus anthracis*, is a Virulence

530   Factor for Anthrax Pathogenesis. *Mol. Microbiol.* **75,** 324–332 (2010).

531   40.   Sleytr, U. B. *et al.* in *Progress in Molecular Biology and Translational Science* **103,** 277–

532   352 (2011).

533   41.   Bingle, W. H., Nomellini, J. F. & Smit, J. Cell-surface Display of a *Pseudomonas*

534   *aeruginosa* Strain K Pilin Peptide within the Paracrystalline S-layer of *Caulobacter*

535   *crescentus*. *Mol. Microbiol.* **26,** 277–288 (1997).

536   42.   Charrier, M. *et al.* Engineering the S-layer of *Caulobacter crescentus* as a Foundation for

537   Stable, High-Density, 2D Living Materials. *ACS Synth. Biol.* acssynbio.8b00448 (2018).

538   doi:10.1021/acssynbio.8b00448

539   43.   Zhou, X., Hu, X., Li, J. & Wang, N. A Novel Periplasmic Protein, VrpA, Contributes to

540   Efficient Protein Secretion by the Type III Secretion System in *Xanthomonas* spp. *Mol.*

541   *Plant-Microbe Interact.* **28,** 143–153 (2015).

542   44.   Walker, S. G., Smith, S. H. & Smit, J. Isolation and Comparison of the Paracrystalline

543   Surface Layer Proteins of Freshwater *Caulobacters*. *J. Bacteriol.* **174,** 1783–1792 (1992).

544   45.   von Diezmann, A., Shechtman, Y. & Moerner, W. E. Three-Dimensional Localization of

545   Single Molecules for Super- Resolution Imaging and Single-Particle Tracking. *Chem. Rev.*

546   **117,** 7244–7275 (2017).

547   46.   Lew, M. D., von Diezmann, A. R. S. & Moerner, W. E. Easy-DHPSF Open-source

548   Software for Three-dimensional Localization of Single Molecules with Precision Beyond

549   the Optical Diffraction Limit. *Protoc. Exch.* (2013). doi:doi:10.1038/protex.2013.026

550   47.   Cignoni, P. *et al.* MeshLab: An Open-source Mesh Processing Tool. *Eurographics Ital.*

551   *Chapter Conf.* 129–136 (2008).

552   doi:10.2312/LocalChapterEvents/ItalChap/ItalianChapConf2008/129-136

553

554   Data Availability Statement

555   Extended data figures (10) are provided with this manuscript, which include representative

556   images from all data sets. Full imaging data sets are available from the corresponding author

557   W.E.M. upon reasonable request.

558

559   Acknowledgements

570

571   Author Contributions

572   Conceptualization: C.J.C., J.H., L.S., S.W., and W.E.M. Investigation: C.F.C., J.H., J.Y., and F.J.

573   Formal analysis: C.J.C., J.H., J.Y., X.Z., and W.E.M. Resources: X.Z., J.N., J.S., and L.S.

574   Writing—original draft: C.J.C. and J.H. Writing—review and editing: All authors. Supervision

575   and funding acquisition: J.S., L.S., S.W., and W.E.M.

576

577   Competing Interests

578   The authors declare no competing financial interests.

579

580   Correspondence and requests for materials should be addressed to S.W. or W.E.M.